Seismic site effects by an optimized 2D BE/FE method

I. Theory, numerical optimization and application to topographical irregularities

B. Gatmiri[1,2], C. Arson[2], K.V. Nguyen[2]

1. University of Tehran, IRAN

2. CERMES, Ecole Nationale des Ponts et Chaussées, Cité Descartes, Champs-sur-Marne, 6-8 avenue Blaise Pascal, 77455 Marne-la-Vallée cedex 2, FRANCE

Tel : (0033) 1 64 15 35 66 or: (0033) 1 64 15 35 24

Fax : (0033) 1 64 15 35 62

gatmiri@cermes.enpc.fr, arson@cermes.enpc.fr

Abstract

This paper deals with the evaluation of seismic site effects due to the local topographical and geotechnical characteristics. The amplification of surface motions is calculated by a numerical method combining finite elements in the near field and boundary elements in the far field (FEM/BEM). The numerical technique is improved by time truncation. In the first part of this article, the accuracy and the relevance of this optimized method are presented. Moreover, parametric studies are done on slopes, ridges and canyons to characterize topographical site effects. The second part deals with sedimentary valleys. The complexity of the combination of geometrical and sedimentary effects is underlined. Extensive parametrical studies are done to

discriminate the topographical and geotechnical effects on seismic ground movement amplifications in two-dimensional irregular configurations. Characteristic coefficients are defined to predict the amplifications of horizontal displacements. The accuracy of this quantitative evaluation technique is tested and discussed.

Key-words

hybrid numerical technique, time truncation, convergence criterion, CPU time, mesh size, elastodynamics, seismic amplification, 2D site effects, topographical irregularities, parametric study

1. Introduction

It has often been reported, after destructive earthquakes in mountain areas, that buildings located at the top of cliffs or hills suffer much more intensive damage than those located at the base. For example, the 1968 Tokachi-Oki earthquake in Japan produced considerable damage to buildings close to the edge of a cliff, contrary to buildings located relatively far from the edge. The 1995 Kozani earthquake in Greece brought the evidence of serious damage for villages built on hills. Particularly, high accelerations were recorded at the crest of the Pacoima Dam (around 1.25 g) during the 1971 San Fernando earthquake in California [32]. Experimental studies dealing with topographical effects are also reported in [17, 21]. A state of the art is also done in [24, 7].

A considerable amount of theoretical work has been reported in the literature of geotechnics and seismology, in order to model, quantify and predict the effects of the basin topography. As the subject is complex, analytical solutions can only be derived for a very limited number of simple configurations. The exact solutions found by Sanchez-Sesma for triangular wedges are exposed in [26, 27]. Analytical solutions for semi-circular and semi-elliptical canyons are presented in [31, 35].

In order to model site effects in more realistic circumstances (for P-SV waves and for a arbitrary shape of topographical feature), numerical methods have to be used. The finite difference method [3, 4, 23], the finite element method [30, 5], the discrete wavenumber method [1, 19], and the boundary element method [34, 25, 29, 33, 20, 28, 2, 24] are the most frequently used. Domain-based methods such as the Finite Element Method (FEM) represent excellent tools in analyzing heterogeneity and non-linearity in the soil. However, the size of the problem can easily exceed computing capacities

and time because of the difficulty of modelling wave propagation in unbounded domains. In recent years, the boundary element methods (BEM), based on the discretization of integral equations, have gained importance in the resolution of wave propagation problems. These techniques can avoid the introduction of fictitious boundaries and reduce the dimensionality of the problem. In order to benefit from the advantages of both domain- and boundary-based methods, the BEM was coupled with the FEM [9] and the finite difference method [6]. Extension of boundary element method to unsaturated porous media has been achieved recently in [13] and [14].

In this paper, the two-dimensional wave scattering due to the presence of topographical irregularities is studied with the aid of a hybrid numerical technique, combining finite elements in the near field and boundary elements in the far field. The program used is HYBRID, developed by Gatmiri and his coworkers [9, 10, 15, 18]. The integration process is approximated in the domain by time truncation [8]. Hence calculations are performed faster, with a good accuracy compared to traditional boundary integration methods. Several types of topography (slope, canyon or ridge) are considered. The role of some key parameters, such as exciting frequency, depth and shape of the relief, are described and discussed.

2. An optimized hybrid numerical technique

2.1. Formulation of problems combining BEM and FEM

The finite-element method (FEM) is particularly adapted to work with anelastic or non linear soils. The boundary-element method (BEM) reduces the problem by one dimension and is relevant for half-plane problems. The study of site effects requires the resolution of mechanical wave radiation equations in irregular configurations, defined by specific topographical and geotechnical conditions. That is why hybrid models combing both methods are often used. In our study, sediments are modelled by finite elements. Substratum is represented by boundary elements, which is adapted to the study in the far field. The region of interest is a half-space and must be enclosed with fictitious boundary elements known as "enclosing elements". All materials are supposed to be elastic.

In the finite-element domain, application of the modified Newton-Raphson iterative method leads to:

$$M \bullet \ddot{U}^{t+\Delta t(k)} + K^t \bullet \left(U^{t+\Delta t(k)} - U^{t+\Delta t(k-1)}\right) = R^{t+\Delta t} - F^{t(k)} \qquad (1)$$

where M is the mass matrix, and K^t is the rigidity matrix at instant t. $U^{t+\Delta t(k)}$ is the displacement vector for the k^{th} iteration done to reach the load increment $R^{t+\Delta t}$ imposed at $t+\Delta t$. $F^{t(k)}$ is the force calculated by the behaviour law of the material at the k^{th} iteration.

Using the Newmark method, in which:

$$U^{t+\Delta t} = U^t + \frac{\Delta t}{2} \cdot \left(\dot{U}^t + \dot{U}^{t+\Delta t} \right) \qquad (2)$$

equation (1) becomes:

$$\overline{K}^t \bullet \Delta U^{(k)} = R^{t+\Delta t} - F^{t(k)} - \left(\frac{4}{(\Delta t)^2} \cdot M \right) \bullet \left(U^{t+\Delta t(k-1)} - U^t \right) + \left(\frac{4}{\Delta t} \cdot M \right) \bullet \dot{U}^t + M \bullet \ddot{U}^t \qquad (3)$$

where:

$$\overline{K}^{t} = K^{t} + \frac{4}{(\Delta t)^2} \cdot M \tag{4}$$

Adding $\overline{K}^{t} \bullet U^{t+\Delta t(k-1)}$ at both sides of equation (3) and assuming that zone 1 is modelled with finite elements:

$$\overline{K}^{t} \bullet U^{t+\Delta t(k)} = R_1^{\,t+\Delta t} - Z_1^{\,t+\Delta t(k)} \tag{5}$$

where:

$$Z_1^{\,t+\Delta t(k)} = F_1^{\,t(k)} - K_1^{\,t} \bullet U_1^{\,t+\Delta t(k-1)} - \left(\frac{4}{(\Delta t)^2} \cdot U_1^{\,t} + \frac{4}{\Delta t} \cdot \dot{U}_1^{\,t} + \ddot{U}_1^{\,t} \right) \bullet M_1 \tag{6}$$

The boundary integral equation of elastodynamics in time-domain for a homogeneous isotropic elastic medium, occupying a volume Ω, bounded by a surface Γ, and subjected to an incident plane wave is:

$$c_{ij}(\xi) \cdot u_j(\xi) = \int_{\Gamma} \left[G_{ij}(\xi, x, t) * t_j(x, t) - F_{ij}(\xi, x, t) * u_j(x, t) \right] \cdot d\Gamma + u_i^{eq}(\xi, t) \tag{7}$$

if the contributions of initial conditions and body forces are neglected. ξ is the source point, x is the field point; u_i and t_i are the amplitudes of the i^{th} component of displacement and traction vectors respectively, at the boundary; u_i^{eq} represents the incident wave; the symbol * indicates a Riemann convolution integral; c_{ij} is the discontinuity term depending on the local geometry of the boundary at ξ and on the Poisson's ratio; G_{ij} and F_{ij} are the fundamental solutions representing the displacement and traction at x in direction *i* due to a unit point force applied at ξ in the *j* direction.

The numerical implementation of equation (7) requires a discretization in both time and space. For this purpose, the boundary Γ is discretized into a defined number of elements, and time axis is divided into *N* equal intervals so that $t = N \cdot \Delta t$.

In this work, quadratic spatial variation of the field variables (displacement and traction) is assumed over each element. Both constant and linear temporal variations can be used for each field variable. Space discretization gives the following matricial expression at instant $t = N \cdot \Delta t$:

$$F^1 \bullet U^N = G^1 \bullet T^N + \sum_{n=1}^{N-1} \left(G^{N+1-n} \bullet T^n - F^{N+1-n} \bullet U^n \right) \tag{8}$$

The equations obtained from the FEM are expressed in force and displacement whereas in the BEM, stresses replace forces. Therefore, equations need to be adapted. In the last term of (8), stresses are transformed into forces as follows:

$$Z^{t(k)} = N \bullet \left(G^1 \right)^{-1} \bullet \sum_{n=1}^{N-1} \left(F^{N+1-n} \bullet U^n - G^{N+1-n} \bullet T^n \right) \tag{9}$$

Consider that zone 2 modelled by boundary elements and has a common frontier with zone 1, which is modelled by finite elements (See 5, 6). The governing matricial equation of zone 2 can be written in the same way as (5):

$$\overline{K}_2^t \bullet U_2^{t+\Delta t(k)} = R_2^{t+\Delta t(k)} - Z'^{t+\Delta t(k)}_2 \tag{10}$$

2.2. Validation of HYBRID program

This study is based on simulations done with HYBRID program. It was developed and validated by Gatmiri and his coworkers. In the far field, the model is based on the direct boundary integration technique [9]. The boundary elements are combined to finite elements, used for the near field representation. Two-dimensional fundamental

solutions have been found out and implemented in HYBRID for saturated porous media [10, 15], and for unsaturated soils [13]. HYBRID also contains a three-dimensional fundamental solution for unsaturated porous materials [14]. The integration process has been approximated in the domain by time truncation [8] (See paragraph 2.3).

HYBRID has been used to analyze the seismic response of topographical irregularities in [11, 12, 18, 16, 15].

2.3. Principles of domain approximation in the fast numerical technique

In [9, 8], it is demonstrated that equation (7) can be written as:

$$\begin{aligned} c_{ij}(\xi)\cdot u_j(\xi) &= \int_\Gamma \left[\int_{t_0}^{t} G_{ij}(\xi,x,t-\tau)\cdot t_j(x,\tau)\cdot d\tau\right]\cdot d\Gamma \\ &- \int_\Gamma \left[\int_{t_0}^{t} F_{ij}(\xi,x,t-\tau)\cdot u_j(x,\tau)\cdot d\tau\right]\cdot d\Gamma + \int_\Omega G_{ij}(\xi,x,t)\cdot F_j^0(x,t)\cdot d\Omega \end{aligned} \tag{11}$$

which can also be expressed as following:

$$\begin{aligned} c_{ij}(\xi)\cdot u_j(\xi) &= \int_\Gamma \left[\int_{t_0}^{t} G_{ij} * t_j(x,\tau)\cdot d\tau\right]\cdot d\Gamma \\ &- \int_\Gamma \left[\int_{t_0}^{t} F_{ij} * u_j(x,\tau)\cdot d\tau\right]\cdot d\Gamma + \int_\Omega G_{ij}\cdot F^0\cdot d\Omega \end{aligned} \tag{12}$$

2.3.1. Meshing method

Equation (12) can be solved by calculating domain integrals at each new time. The first two equations are:

$$c \cdot u_1 = \int_\Gamma \left[\int_{t_0}^{t_1} G_{ij} * t_j(x,\tau) \cdot d\tau \right] \cdot d\Gamma - \int_\Gamma \left[\int_{t_0}^{t_1} F_{ij} * u_j(x,\tau) \cdot d\tau \right] \cdot d\Gamma + \int_\Omega G_{ij}^1 \cdot F^0 \cdot d\Omega \quad (13)$$

$$c \cdot u_2 = \int_\Gamma \left[\int_{t_1}^{t_2} G_{ij} * t_j(x,\tau) \cdot d\tau \right] \cdot d\Gamma - \int_\Gamma \left[\int_{t_1}^{t_2} F_{ij} * u_j(x,\tau) \cdot d\tau \right] \cdot d\Gamma + \int_\Omega G_{ij}^1 \cdot F^1 \cdot d\Omega \quad (14)$$

If time intervals are equal, boundary integral coefficients are also equal, and need thus to be calculated only once (Fig. 1). Forces defined in the domain are evaluated at nodes or at Gauss integration points. This process has to be repeated for each position of the source point on the boundary, which is rather complicated and time-consuming.

2.3.2. Wrobel method

This method requires the storage of all the boundary integral coefficients from the beginning of time discretization to current time:

$$c \cdot u_1 = \int_\Gamma \left[\int_{t_0}^{t_1} G_{ij} * t_j(x,\tau) \cdot d\tau \right] \cdot d\Gamma - \int_\Gamma \left[\int_{t_0}^{t_1} F_{ij} * u_j(x,\tau) \cdot d\tau \right] \cdot d\Gamma + \int_\Omega G_{ij}^1 \cdot F^0 \cdot d\Omega \quad (15)$$

$$c \cdot u_2 = \int_\Gamma \left[\int_{t_0}^{t_2} G_{ij} * t_j(x,\tau) \cdot d\tau \right] \cdot d\Gamma - \int_\Gamma \left[\int_{t_0}^{t_2} F_{ij} * u_j(x,\tau) \cdot d\tau \right] \cdot d\Gamma + \int_\Omega G_{ij}^2 \cdot F^0 \cdot d\Omega \quad (16)$$

Assuming that time intervals are equal, some integral coefficients are also equal (Fig. 2). This procedure avoids domain discretization, but requires the storage and the manipulation of large amounts of data. CPU time needed for the calculation of forces, from one interval to the next, increases with the number of time iterations.

2.3.3. Time-truncation method

This fast integration process is exposed in [8]. The method consists of a domain approximation based on time truncation. Integration is limited to a number of time steps (m) chosen at the beginning of the calculation (Fig. 3). Consider the case $m = 3$. The first three equations are similar to the ones used in the Wrobel method. The third equation is thus:

$$\begin{aligned} c \cdot u_3 &= \int_\Gamma \left[\int_{t_0}^{t_3} G_{ij} * t_j(x,\tau) \cdot d\tau \right] \cdot d\Gamma \\ &- \int_\Gamma \left[\int_{t_0}^{t_3} F_{ij} * u_j(x,\tau) \cdot d\tau \right] \cdot d\Gamma + \int_\Omega G_{ij}^3 \cdot F^0 \cdot d\Omega \end{aligned} \tag{17}$$

If the number of time steps is fixed to $m-1$, the third equation is:

$$\begin{aligned} c \cdot u_3 &= \int_\Gamma \left[\int_{t_1}^{t_3} G_{ij} * t_j(x,\tau) \cdot d\tau \right] \cdot d\Gamma \\ &- \int_\Gamma \left[\int_{t_1}^{t_3} F_{ij} * u_j(x,\tau) \cdot d\tau \right] \cdot d\Gamma + \int_\Omega G_{ij}^2 \cdot F^1 \cdot d\Omega \end{aligned} \tag{18}$$

Comparing equations (17) and (18) yields to the following:

$$\begin{aligned} &\int_\Omega G_{ij}^2 \cdot F^1 \cdot d\Omega = \int_\Omega G_{ij}^3 \cdot F^0 \cdot d\Omega \\ &\int_\Gamma \left[\int_{t_0}^{t_1} G_{ij} * t_j(x,\tau) \cdot d\tau \right] \cdot d\Gamma - \int_\Gamma \left[\int_{t_0}^{t_1} F_{ij} * u_j(x,\tau) \cdot d\tau \right] \cdot d\Gamma \end{aligned} \tag{19}$$

The fourth equation cannot be evaluated, unless the domain integral can be calculated:

$$\begin{aligned} c \cdot u_4 &= \int_\Gamma \left[\int_{t_1}^{t_4} G_{ij} * t_j(x,\tau) \cdot d\tau \right] \cdot d\Gamma \\ &- \int_\Gamma \left[\int_{t_1}^{t_4} F_{ij} * u_j(x,\tau) \cdot d\tau \right] \cdot d\Gamma + \int_\Omega G_{ij}^3 \cdot F^1 \cdot d\Omega \end{aligned} \tag{20}$$

The known value of the domain integral on the left-hand side of equation (19) is used to approximate the unknown domain integral of equation (20). The generalized mean value theorem yields:

$$\int_{\Omega} G_{ij}^{2} \cdot F^{1} \cdot d\Omega = \overline{F_1} \bullet \int_{\Omega} G_{ij}^{2} \cdot d\Omega \tag{21}$$

and

$$\int_{\Omega} G_{ij}^{3} \cdot F^{1} \cdot d\Omega = \left(\overline{F_1} + \eta\right) \bullet \int_{\Omega} G_{ij}^{3} \cdot d\Omega \tag{22}$$

where

$$\overline{F_1} = \left[\int_{\Omega} G_{ij}^{2} \cdot d\Omega\right]^{-1} \bullet \int_{\Omega} G_{ij}^{2} \cdot F^{1} d\Omega \tag{23}$$

The average value of body forces $\overline{F_1}$ can be calculated from equation (19). Assuming η to be zero in equation (22) leads to the following approximation:

$$\int_{\Omega} G_{ij}^{3} \cdot F^{1} \cdot d\Omega \approx \left[\int_{\Omega} G_{ij}^{2} \cdot d\Omega\right]^{-1} \bullet \int_{\Omega} G_{ij}^{2} \cdot F^{1} d\Omega \bullet \int_{\Omega} G_{ij}^{3} \cdot d\Omega \tag{24}$$

In the fifth equation, the domain integral is

$$\int_{\Omega} G_{ij}^{3} \cdot F^{2} \cdot d\Omega \tag{25}$$

which can be approximated by means of the generalized mean value theorem:

$$\int_{\Omega} G_{ij}^{3} \cdot F^{2} \cdot d\Omega \approx \overline{F_2} \bullet \int_{\Omega} G_{ij}^{3} \cdot d\Omega \tag{26}$$

where

$$\overline{F_2} = \left[\int_{\Omega} G_{ij}^{2} \cdot d\Omega\right]^{-1} \bullet \int_{\Omega} G_{ij}^{2} \cdot F^{2} d\Omega \tag{27}$$

The equation at the fourth time step provides the missing domain integral value:

$$\begin{aligned} &\int_{\Omega} G_{ij}^{2} \cdot F^{2} \cdot d\Omega = \int_{\Omega} G_{ij}^{3} \cdot F^{1} \cdot d\Omega \\ &\int_{\Gamma}\left[\int_{t_1}^{t_2} G_{ij} * t_j(x,\tau) \cdot d\tau\right] \cdot d\Gamma - \int_{\Gamma}\left[\int_{t_1}^{t_2} F_{ij} * u_j(x,\tau) \cdot d\tau\right] \cdot d\Gamma \end{aligned} \tag{28}$$

It can be seen that for $m = 3$, calculations at the fifth time step need two successive approximations.

2.4. General formulation of the improved integration method

Assuming that the number of time steps chosen for the integration approximation sums to m, the N^{th} equation is expressed as:

$$\begin{aligned} c \cdot u_N &= \int_\Gamma \left[\int_{t_{N-m}}^{t_N} G_{ij} * t_j(x,\tau) \cdot d\tau \right] \cdot d\Gamma \\ &- \int_\Gamma \left[\int_{t_{N-m}}^{t_N} F_{ij} * u_j(x,\tau) \cdot d\tau \right] \cdot d\Gamma + \int_\Omega G_{ij}^m \cdot F^{N-m} \cdot d\Omega \end{aligned} \tag{29}$$

The domain integral can only be approximated as:

$$\int_\Omega G_{ij}^m \cdot F^{N-m} \cdot d\Omega \approx \psi_m \bullet \int_\Omega G_{ij}^{m-1} \cdot F^{N-m} \cdot d\Omega \tag{30}$$

where:

$$\psi_m \approx \left[\int_\Omega G_{ij}^{m-1} \cdot d\Omega \right]^{-1} \bullet \int_\Omega G_{ij}^m \cdot d\Omega \tag{31}$$

Writing equation (29) at the instant $t = (N-1) \cdot \Delta t$ for m and $m-1$ yields:

$$\begin{aligned} \int_\Omega G_{ij}^{m-1} \cdot F^{N-m} \cdot d\Omega &= \int_\Gamma \left[\int_{t_{N-m-1}}^{t_{N-m}} G_{ij} * t_j(x,\tau) \cdot d\tau \right] \cdot d\Gamma \\ &- \int_\Gamma \left[\int_{t_{N-m-1}}^{t_{N-m}} F_{ij} * u_j(x,\tau) \cdot d\tau \right] \cdot d\Gamma + \int_\Omega G_{ij}^m \cdot F^{N-m-1} \cdot d\Omega \end{aligned} \tag{32}$$

The same thing can be done at $t = (N-2) \cdot \Delta t$:

$$\begin{aligned} \int_\Omega G_{ij}^{m-1} \cdot F^{N-m-1} \cdot d\Omega &= \int_\Gamma \left[\int_{t_{N-m-2}}^{t_{N-m-1}} G_{ij} * t_j(x,\tau) \cdot d\tau \right] \cdot d\Gamma \\ &- \int_\Gamma \left[\int_{t_{N-m-2}}^{t_{N-m-1}} F_{ij} * u_j(x,\tau) \cdot d\tau \right] \cdot d\Gamma + \int_\Omega G_{ij}^m \cdot F^{N-m-2} \cdot d\Omega \end{aligned} \tag{33}$$

Using (29), (30) and (32) yields:

$$
\begin{aligned}
c\cdot u_N \approx & \int_\Gamma\left[\int_{t_{N-m}}^{t_N} G_{ij} * t_j(x,\tau)\cdot d\tau\right]\cdot d\Gamma - \int_\Gamma\left[\int_{t_{N-m}}^{t_N} F_{ij} * u_j(x,\tau)\cdot d\tau\right]\cdot d\Gamma \\
& + \psi_m \bullet \left[\int_\Gamma\left[\int_{t_{N-m-1}}^{t_{N-m}} G_{ij} * t_j(x,\tau)\cdot d\tau\right]\cdot d\Gamma - \int_\Gamma\left[\int_{t_{N-m-1}}^{t_{N-m}} F_{ij} * u_j(x,\tau)\cdot d\tau\right]\cdot d\Gamma\right] \\
& + \psi_m \bullet \int_\Omega G_{ij}^m \cdot F^{N-m-1}\cdot d\Omega
\end{aligned}
\tag{34}
$$

Approximating the domain integral in equation (32) results in:

$$
\begin{aligned}
\int_\Omega G_{ij}^{m-1}\cdot F^{N-m}\cdot d\Omega \approx & \int_\Gamma\left[\int_{t_{N-m-1}}^{t_{N-m}} G_{ij} * t_j(x,\tau)\cdot d\tau\right]\cdot d\Gamma \\
& - \int_\Gamma\left[\int_{t_{N-m-1}}^{t_{N-m}} F_{ij} * u_j(x,\tau)\cdot d\tau\right]\cdot d\Gamma + \psi_m \bullet \int_\Omega G_{ij}^{m-1}\cdot F^{N-m-1}\cdot d\Omega
\end{aligned}
\tag{35}
$$

Rewriting equation (34), by equations (29), (30), (33) and (35) leads to the following relationship:

$$
\begin{aligned}
c\cdot u_N \approx & \int_\Gamma\left[\int_{t_{N-m}}^{t_N} G_{ij} * t_j(x,\tau)\cdot d\tau\right]\cdot d\Gamma - \int_\Gamma\left[\int_{t_{N-m}}^{t_N} F_{ij} * u_j(x,\tau)\cdot d\tau\right]\cdot d\Gamma \\
& + \psi_m \bullet \left[\int_\Gamma\left[\int_{t_{N-m-1}}^{t_{N-m}} G_{ij} * t_j(x,\tau)\cdot d\tau\right]\cdot d\Gamma - \int_\Gamma\left[\int_{t_{N-m-1}}^{t_{N-m}} F_{ij} * u_j(x,\tau)\cdot d\tau\right]\cdot d\Gamma\right] \\
& + (\psi_m)^2 \bullet \left[\int_\Gamma\left[\int_{t_{N-m-2}}^{t_{N-m-1}} G_{ij} * t_j(x,\tau)\cdot d\tau\right]\cdot d\Gamma - \int_\Gamma\left[\int_{t_{N-m-2}}^{t_{N-m-1}} F_{ij} * u_j(x,\tau)\cdot d\tau\right]\cdot d\Gamma\right] \\
& + (\psi_m)^2 \bullet \int_\Omega G_{ij}^m \cdot F^{N-m-2}\cdot d\Omega
\end{aligned}
\tag{36}
$$

Repeating the process till the domain integral affects the initial forces at $t = t_0$, yields:

$$
\begin{aligned}
c\cdot u_N \approx & \int_\Gamma\left[\int_{t_{N-m}}^{t_N} G_{ij} * t_j(x,\tau)\cdot d\tau\right]\cdot d\Gamma - \int_\Gamma\left[\int_{t_{N-m}}^{t_N} F_{ij} * u_j(x,\tau)\cdot d\tau\right]\cdot d\Gamma \\
& + \sum_{i=1}^{N-m}(\psi_m)^i \bullet \left[\begin{array}{l} \displaystyle\int_\Gamma\left[\int_{t_{N-m-i}}^{t_{N-m-i+1}} G_{ij} * t_j(x,\tau)\cdot d\tau\right]\cdot d\Gamma \\ \displaystyle -\int_\Gamma\left[\int_{t_{N-m-i}}^{t_{N-m-i+1}} F_{ij} * u_j(x,\tau)\cdot d\tau\right]\cdot d\Gamma \end{array}\right] \\
& + (\psi_m)^{N-m} \bullet \int_\Omega G_{ij}^m \cdot F^0\cdot d\Omega
\end{aligned}
\tag{37}
$$

When $\psi_m < 1$, $\lim_{i\to+\infty}(\psi_m)^i = 0$. It is possible to ignore the time steps at a certain distance from the limit of backtracking. The integration process continues until a convergence criterion $(\psi_m)^q < L_m$ is satisfied for some small tolerance L_m. In other words, the time integration is truncated after $m+q$ steps $(m+q<N)$ and the determination of the current state requires only the knowledge of $m+q$ former states. Therefore, computation time decreases considerably. Moreover, only the first $m+q$ pairs of coefficients (G_{uj}, F_{ij}) need to be stored instead of all N pairs, which reduces temporary storage requirement. The formulation is only an approximation; whose precision is controlled by the tolerance L_m and by the number of time steps m. In the half-plane problems treated in the following examples, m and L_m are selected to be equal 5 and 0.1 respectively, which gives a reasonable precision.

2.5. Optimized hybrid method testing

2.5.1. Accuracy of the calculations

The diffraction of a plane SV wave of vertical incidence by a semi-circular canyon is studied for an elastic half-plane. The Poisson ratio is $\nu = 1/3$ and the dimensionless frequency η of the input signal equals 2. The dimensionless frequency η is the ratio of the characteristic dimension of the relief to the wavelength:

$$\eta = \frac{f \cdot L_C}{c} = \frac{L_C}{\lambda} \tag{38}$$

f and λ are the frequency and the wavelength of the signal respectively; c is the wave velocity; L_C is the characteristic dimension of the geometry (in this example,

L_C is the diameter of the canyon). The horizontal and vertical motion amplitudes given by the time truncation method are compared with the results obtained by other authors. Amplitudes are normalized by the displacement measured on the outcrop. Fig. 4 shows an excellent agreement between the diverse modelling techniques.

The validation of the optimized method must be completed to check if the motions are at the good scale of sizes. Define amplification by the ratio of the amplitude of the wave observed at the surface of the topography to the amplitude of the incident wave. The amplification at a free surface modelled with boundary elements and submitted to a real seismogram turns out to be equal to two, which is in agreement with the theory (Fig. 5 and 6).

2.5.2. Efficiency of the method

The domain approximation technique has been compared to the traditional integration method. In [8], an elastic trapezoidal ridge is studied. The topography and the straight half-space are modelled with eight-node finite elements and three-node boundary elements respectively. The incident excitation is a Ricker SV wave propagating vertically. The central frequency is equal to 3 Hz. Horizontal displacements are compared at a point of the axis (Fig. 7) and at an edge (Fig. 8). Both methods provide very similar results. Moreover, the calculation lasts three hours by the exact method, whereas it is only fifteen minutes long by the optimized method if $m = 5$. Accuracy and efficiency of the time truncation technique are thus demonstrated.

2.5.3. Elimination of artificial waves induced by spatial truncation of the model

Half-plane configurations are modelled with finite-size meshes, whose extreme points are diffracting. Surface waves can propagate from the edges to the centre of the studied

topography. A solution consists in introducing absorbing boundaries. At the border of the model, assuming that the incident wave propagation is vertical, stresses must satisfy the following equations:

$$\begin{cases} \sigma_{nn} = \rho \cdot c_L \cdot \partial_t \vec{u} \bullet \vec{n} \\ \tau = \rho \cdot c_T \cdot \partial_t u_T \end{cases} \quad (39)$$

Assuming that the model is two-dimensional, σ_{nn} and τ are the normal and tangential stresses respectively. ρ is the material's volumetric mass. c_L and c_T are the longitudinal and transversal wave velocities respectively. $\vec{u}$ is the displacement vector. $\rho \cdot c_L$ and $\rho \cdot c_T$ are dampers. If the propagation direction changes, equations (39) are more complex. However, in static cases, $\omega = 0$, so $\partial_t \vec{u}$ is equal to zero, and the stresses calculated from (39) vanish. Therefore, an alternative has to be found to the absorbing boundary technique.

In the domain approximation technique, artificial waves emitted at early times (far history) vanish by time truncation. Thus, the centre of the model is not affected by noises. Fig. 9 shows the relevance of the optimized method.

The meshing extension controls the time taken by artificial waves to reach the centre of the model. The required spatial size depends on the time window chosen for the study and needs to be large enough so that diffracted surface waves are attenuated before arriving in the central zone. Time truncation limits the width of the time interval taken into account in the boundary integration process. That is why the discretized zone can be less extended in models based on the domain approximation method. Its size is nearly independent of the width of the time window. The influence of spatial truncation is studied on trapezoidal hills in [16], on the model presented in paragraph 2.5.2. Two types of mesh patterns are considered: one extended up to a distance of 2100 m from the base of the hill, which is far away enough for the considered time

interval $t \in [0, 0.7s]$, and the other up to only 400 m. For the smaller model, calculations are done by both the exact and the approximated methods. Fig. 10 represents the vertical normalized displacement at the centre of the ridge. As can be seen, results provided by the traditional boundary integration method strongly depend on mesh truncation. However, the motion amplitudes calculated by the fast method are in agreement with the ones calculated with the traditional method on a large-extended model. In other words, the time truncation technique provides reliable results using less CPU time and storage requirements, and less extended meshes.

3. Parametrical studies about topographical site effects in 2D configurations

In the following paragraphs, parametric studies are done by means of the hybrid numerical technique, optimized by time truncation, presented in section 2. The aim of this work is to characterize site effects in diverse topographical configurations. Calculations have been done on slopes, canyons, and ridges. The main geometrical variables of interest in this parametric study are given on Fig. 11. Site effects are evaluated on horizontal and vertical surface displacements.

Influence of topography on the seismic response of a half-space is studied in [22]. The soil is assumed to be isotropic, homogeneous and linear elastic: shear wave velocity $c_T = 1$, Poisson ratio $\nu = 0.3$ and mass density $d = 1$. The input signal is a monochromatic plane SV wave propagating vertically. The frequency of the incident

wave is normalized: the dimensionless frequency η (38) is used with $L_C = H$ for a slope (height), and $L_C = L$ for a canyon or a ridge (half-width).

The curves illustrating this part present spatial variation of spectral superficial displacements. Displacement amplitudes are normalized by the amplitude of the incident wave: $ux = 2$ and $uy = 0$ correspond to the response of a half-space, thus $ux > 2$ means an amplification and $ux < 2$ means an attenuation of ground motion.

Ridges and canyons present inversed amplification curves for the horizontal component of surface displacements (Fig. 12). At a fixed observation point (x/L), an amplification observed at the surface of a canyon corresponds to an attenuation at the surface of a ridge, and vice versa. The salient characteristic of site effects by ridges is that the motion at the crest of the ridge is always amplified, due to wave focusing in convex relieves. The phenomenon is explained in [26]. In a SH wave field, horizontal displacement amplitudes at the top of a ridge whose crest angle is $n \cdot \pi$ reaches 1/n times the one at the free surface. If the propagation direction of incident waves is vertical, the maximal amplification is equal to 2/n and is reached on the crest, where reflected waves are in phase. Thus, waves interfere positively, whatever the exciting frequency is. If incident waves propagate obliquely, amplification can be upper than 2/n on the side of the ridge which is the furthest from the source.

3.1. Influence of the dimensionless frequency

At low frequencies, ($\eta < 0.25$ for slopes and $\eta < 1$ for canyons and ridges), seismic ground motion is amplified at the crest of ridges, at the upper corner of slopes and at the edges of canyons. It is systematically attenuated at relief bases. If the exciting

frequency is low enough, the topographical irregularity can be regarded as a small obstacle; its effects on ground motion may thus be neglected.

In general, the higher the exciting frequency, the more significant and complex are topographical site effects. Increasing the exciting frequency also makes the zone of influence of the relief wider, especially if the wavelengths are comparable or lower than the characteristic dimension L_C of the topography. The movement at the bottom of canyons and at the foot of ridges may be amplified. At high frequencies, response spectra are complex. The peaks and depressions are more numerous and do not correspond to the ones observed at lower frequencies. These significant differential motions are caused by the superposition of the incident wave, the refracted waves and the Rayleigh surface waves.

For slopes (Fig. 13.a), it seems that the location of the minimal horizontal displacement shifts towards the upper corner when the frequency of the input motion increases. Similarly, the peak amplitude of the horizontal displacement is not found any more at the crest of the slope, but somewhere nearby. In addition, it is not possible to detect, in the considered interval $\frac{x}{0.5H} \in [-7,+7]$, the location where the movement of the site approaches that of the half-space; this location must be very far from the slope. Vertical displacements on slopes (Fig. 13.b) increase with the exciting frequency. The peak can reach a maximum value comparable to the amplitude of horizontal displacements ($\eta = 0.5$).

The density of peaks and depressions in the response spectra of the canyons increases with the exciting frequency (Fig. 13.c and 13.d). However, amplification effect is more prominent. At high frequencies $(\eta = 1;1.5;2)$, the peak values of horizontal and vertical surface displacements are comparable. In other words, if the dimensionless

frequency keeps on increasing, it can be assumed that the peak value of the motion amplitudes will not change much but the spectrum of the ground motion will become more complex.

Displacements at the crest of the ridges are amplified whatever the frequency of the excitation is, due to the focusing of waves inside the ridge, as mentioned before.

3.2. Influence of slope and depth

Wave focusing in convexities is one of the physical phenomenon generating topographical effects. Another important aspect is the interference of incident volume plane waves with diffracted surface waves. The velocity of Rayleigh waves is not as large as the one of shear waves. The surface waves are less delayed if the canyon is deep and/or steep. Interferences have thus more chances to occur in deep or stiff-sloped relieves.

Amplification at the upper corner of a slope and attenuation at the foot of a slope increase with the inclination angle. The statement is true for both horizontal and vertical components of the surface displacement (Fig. 14).

The depth of the canyon accentuates amplification at the edges and attenuation at the bottom (Fig. 15).

3.3. Influence of the geometrical shape

An attenuation of horizontal displacements at the bottom and a slight amplification at the edges are observed for every canyon shape (Fig. 16.a). For relieves of same

dimensions, the triangular form is the least critical while the rectangular form is the most critical case. It is in agreement with the results presented in paragraph 3.2. The steeper the slope, the huger are site effects.

Due to the symmetry of the configuration, the vertical component is equal to zero at the bottom of a canyon and is non-zero elsewhere. On the free surfaces outside the canyon, vertical displacements vary only slightly (Fig. 16.b).

4. Conclusion

Site effects have been studied by means of HYBRID, a hybrid numerical program combining finite elements in the near field and boundary elements in the far field. Integrals in the domain are approximated by time truncation. Precision is controlled by two parameters: a number of time steps gives the backtracking limit, and a tolerance coefficient cuts the calculation when the terms become negligible. This numerical technique is fast and accurate. Moreover, artificial waves generated at the truncation points of the model vanish easier if the optimized method is used.

Several parametric studies based on this fast hybrid numerical technique have been used to find out the main characteristics of topographical site effects. In absence of sediment, ground motion is generally amplified at the crest of ridges, at the upper corner of slopes and at the edges of canyons. It is systematically attenuated at the base of these relieves. At a distance depending on the exciting frequency and on the dimensions of the topography, the response of the site approaches that of the half-space. Steep slopes and rectangular shapes make topographical effects more critical. At

high exciting frequencies, topographical effects are complex and ground movement amplifications get higher.

The amplification phenomena caused by the presence of a one-dimensional sedimentary layer is well-known. The analysis of the geotechnical contribution to site effects is more complex in two-dimensional configurations. The superposition of the influences of geometry and stratigraphy makes it difficult to identify the more prominent parameters. In the second part of this paper, parametric studies using the same numerical technique are done in order to discriminate site effects due topographical irregularities and site effects due to alluvial filling. A predictive calculation process is also defined in order to evaluate the amplification of surface horizontal displacements in sedimentary valleys.

Appendix

c wave velocity

c_L longitudinal wave velocity

c_T transversal wave velocity

c_{ij} discontinuity term depending on the local geometry of the boundary at ξ and on the Poisson's ratio

f frequency of the input signal

m number of time steps limiting the integration process in the domain by the time-truncation method

q tolerance coefficient limiting the number of iterations in the calculation of $c \cdot u_N$ in the time-truncation technique: $\psi_m^q < L_m$

t_i amplitude of the i^{th} component of the traction vector at the boundary

u_i amplitude of the i^{th} component of the displacement vector at the boundary

ux maximal amplitude of ground displacements in x-direction

uy maximal amplitude of ground displacements in y-direction

x abscissa of the observation point

$F^{t(k)}$ force calculated by the behavior law of the material at the k^{th} iteration

F_{ij} fundamental solution representing the traction at *x* in direction *i* due to a unit point force applied at ξ in the *j*-direction

G_{ij} fundamental solution representing the displacement at *x* in direction *i* due to a unit point force applied at ξ in the *j*-direction

H height of a slope or depth of a canyon

K^t rigidity matrix at instant t

L half-width at the surface of a canyon

L_1 half-width at the base of a canyon

L_C characteristic dimension of the geometry: $L_C = H$ for a slope (height), and $L_C = L$ for a canyon or a ridge (half-width)

L_m convergence criterion used in the time-truncation technique

M mass matrix

N number of intervals dividing the time axis so that $t = N \cdot \Delta t$

$R^{t+\Delta t}$ load increment imposed at $t + \Delta t$

$U^{t+\Delta t(k)}$ displacement vector for the k^{th} iteration done to reach the load increment $R^{t+\Delta t}$ imposed at $t + \Delta t$

α characteristic inclination angle of the topography

ξ source point

η dimensionless frequency

λ wavelength of the input signal

ν Poisson's ratio

ρ volumetric mass

σ_{nn} normal stress

τ tangential stress

x field point

ψ_m scalar parameter used to control the number of iterations in the calculation of domain integrals by the time-truncation technique, for m time steps:

$$\psi_m = \left[\int_\Omega G_{ij}^{\,m-1} \cdot d\Omega \right]^{-1} \bullet \int_\Omega G_{ij}^{\,m} \cdot d\Omega$$

References

[1] Bard P-Y. Diffracted waves and displacement field over two-dimensional elevated topographies. Geophys J R Astr Soc 1982; 71:731-760.

[2] Barros, Luco. Amplification of Obliquely Incident Waves by a Cylindrical Valley Embedded in a Layered Half-Space. Earthquake Engineering and Structural Dynamics 1995; 24:163 – 175.

[3] Boore DM A note on the effect of simple topography on seismic SH waves. Bulletin of the seismological society of America 1972; 62:275-284.

[4] Boore DM, Harmsen S, Harding, S. Wave scattering from a steep change in surface topography. Bulletin of the seismological society of America 1981; 71:117–125.

[5] Castellani A, Peano A., Sardella L. On analytical and numerical techniques for seismic analysis of topographic irregularities. In: Proc of the 7th European Conf Earthquake. Eng. Athens, Greece, 1982, 2:415–423.

[6] Cole DM, Kosloff DD, Bernard J. A numerical boundary integral equations for elastodynamics. Bulletin of the seismological society of America 1978; 68:1331-1357.

[7] Faccioli, Vanini, Frassine. Complex Site Effects in Earthquake Ground Motion, Including Topography. In: Proc of the 12th European Conference on Earthquake Engineering. London, United Kingdom, 2002. Paper reference: 844.

[8] Gatmiri B, Dehghan K. Applying a new fast numerical method to elasto-dynamic transient kernels in HYBRID wave propagation analysis. In: Proc of 6th Conference on Structural Dynamics (EURODYN 2005). Paris, France, 2005. Millpress, Rotterdam, 1879-1884.

[9] Gatmiri B, Kamalian M. Two-Dimensional transient Wave Propagation in Anelastic Saturated Porous Media by a Hybrid FE/BE Method. In: Proc of the 5th European Conference of Numerical Methods in Geotechnical Engineering. Paris, France, 2002, 947-956.

[10] Gatmiri B, Kamalian M. On the fundamental solution of dynamic poroelastic boundary integral equations in the time domain. International Journal of Geomechanics 2002; 2(4):381-398.

[11] Gatmiri B, Kamalian M, Karimi M, Sohrabi A. Seismic Analysis of 2-dimensional Response of Canyons in time domain. In: Proc of the 4th International Conference on Seismology and Earthquake Engineering. 2003.

[12] Gatmiri B, Karimi M, Jafari M. Two-Dimensional Analysis of Topographic Irregularities in Time Domain. In: Proc of the 13th World Conference on Earthquake Engineering. Vancouver, Canada, 2004.

[13] Gatmiri B, Jabbari E. Time-domain Green's functions for unsaturated soils, part I: two dimensional solution. International Journal of Solid and Structure 2005; 42(23):5971-5990.

[14] Gatmiri B, Jabbari E. Time-domain Green's functions for unsaturated soils, part II: three dimensional solution. International Journal of Solid and Structure 2005; 42(23):5991-6002.

[15] Gatmiri B, Nguyen KV. Time 2D Fundamental solution for Saturated Porous Media with Incompressible Fluid. International Journal of Communications in Numerical Methods in Engineering 2005; 21:119-132.

[16] Gatmiri B, Nguyen KV, Dehghan K. Seismic Response of Slopes subjected to incident SV Wave by an Improved Boundary Element Approach. Accepted for publication in International Journal for Numerical and Analytical Methods in Geomechanics.

[17] Geli L, Bard P-Y, Jullien B. The effect of topography on earthquake ground motion: a review and new results. Bulletin of the seismological Society of America 1988; 78:42-63.

[18] Kamalian M, Jafari MK, Sohrabi-Bidar A, Razmkhah A, Gatmiri B. Time-Domain Two-Dimensional Site Response Analysis of Non-Homogeneous Topographic Structures by A Hybrid FE/BE Method. International Journal of Soil Dynamics and Earthquake Engineering 2006; 26(8):753-765.

[19] Kawase H. Time-domain response of a semi-circular canyon for incident SV, P and Rayleigh waves calculated by the discrete wavenumber boundary element method. Bulletin of the seismological Society of America 1988; 78:1415-1437.

[20] Luco, Wong, Barros. 3D Response of a Cylindrical Canyon in a Layered Half-Space. Earthquake Engineering and Structural Dynamics 1990; 19: 799 – 817.

[21] Nechtschein S, Bard P-Y, Gariel J-C, Meneroud J-P, Dervin P, Cushing M, Gaubert B, Vidal S, Duval A-M. A topographic effect study in the Nice region. In: Proc of the 5th International Conference on seismic zonation. Nice, France, 1995, 1067-1074.

[22] Nguyen KV, Gatmiri B. Evaluation of seismic ground motion induced by topographic irregularities. Accepted for publication in International Journal of Soil Dynamics and Earthquake Engineering.

[23] Ohtsuki, Karumi. Effects of Topography and Subsurface Inhomogeneities on Seismic SV Waves. Earthquake Engineering and Structural Dynamics 1983; 11:441 – 462.

[24] Reinoso, Wrobel, Power. 3D Scattering of Seismic Waves from Topographical Structures. Soil Dynamics and Earthquake Engineering 1997; 16:41 – 61.

[25] Sanchez-Sesma F-J. Ground motion amplification due to canyons of arbitrary shape, in Proc of the 2nd International Conference on Microzonation. San Francisco, California, 1978, 729-738.

[26] Sanchez-Sesma F-J. Diffraction of Elastic SH Waves by Wedges. Bulletin of the seismological society of America 1985; 75:1435-1446.

[27] Sanchez-Sesma F-J. Site Effects on Strong Ground Motion. Soil Dynamics and Earthquake Engineering 1987; 6(2).

[28] Sanchez-Sesma F-J, Campillo M. Diffraction of P, SV and Rayleigh waves by topographic features: a boundary integral formulation. Bulletin of the seismological Society of America 1991; 81(6):2234-2253.

[29] Sanchez-Sesma F-J, Herrera I, Aviles J. A boundary method for elastic wave diffraction: application to scattering waves by surface irregularities. Bulletin of the seismological Society of America 1982; 72:473-490.

[30] Smith WD. The application of finite element analysis to elastic body wave propagation problems. Geophys J R Astr Soc 1975; 42:747-768.

[31] Trifunac MD. Scattering of plane SH waves by a semi-cylindrical canyon. International Journal for Earthquake Engineering and Structural Dynamics 1973; 1:267–281.

[32] Trifunac MD, Hudson DE. Analysis of the Pacoima Dam accelerogram - San Fernando, California, earthquake of 1971. Bulletin of the seismological Society of America 1971; 61:1393-1411.

[33] Vogt RF, Wolf JP, Bachmann H. Wave scattering by a canyon of arbitrary shape in a layered half-space. International Journal for Earthquake Engineering and Structural Dynamics 1988; 16:803-812.

[34] Wong H, Jennings P. Effect of canyon topographies on strong ground motion. Bulletin of the seismological Society of America 1975; 65:1239–1257.

[35] Wong H, Trifunac MD. Scattering of plane SH waves by a semi-elliptical canyon. International Journal for Earthquake Engineering and Structural Dynamics 1974; 3:157–169.

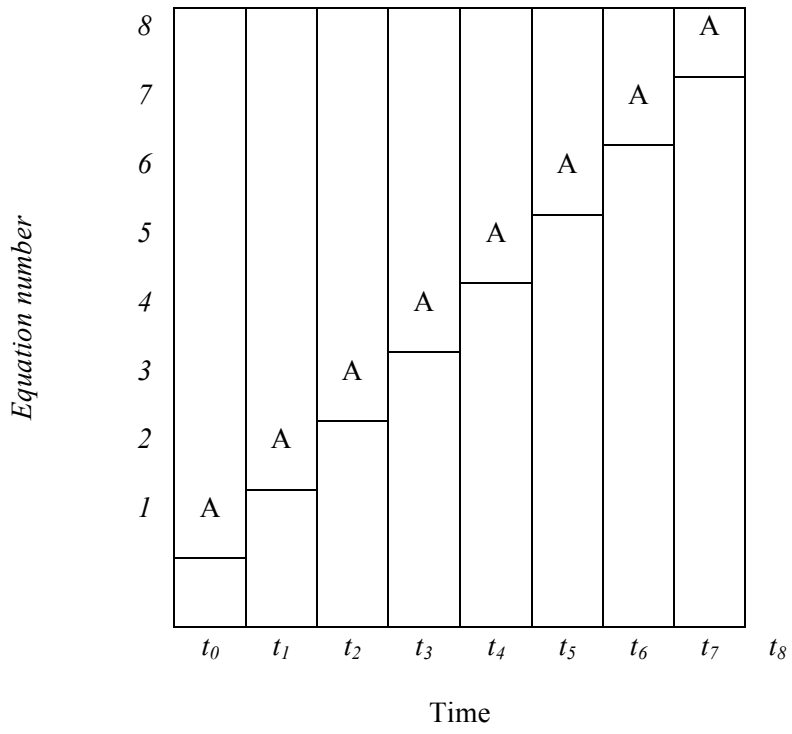

Figure 1: Integration limits – meshing method

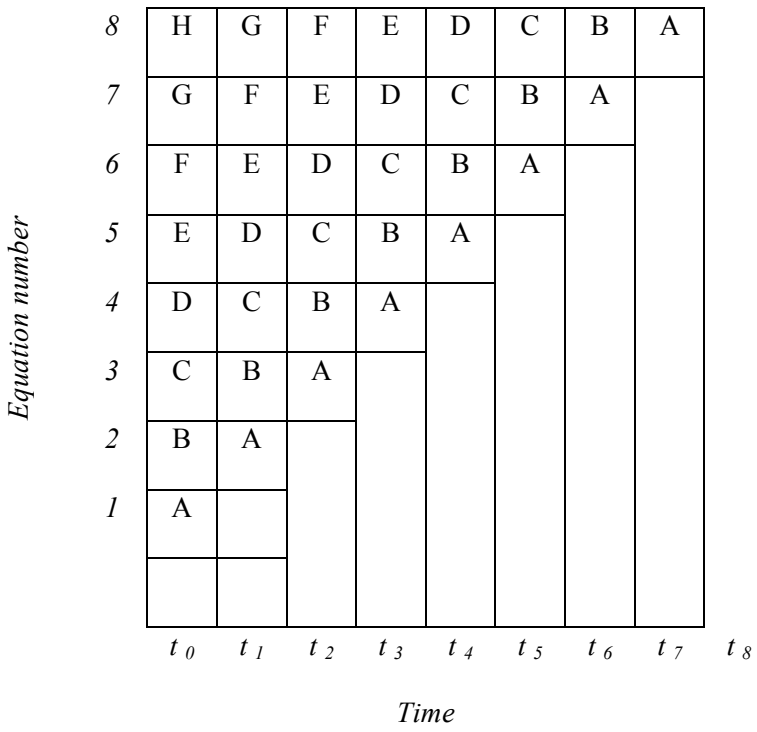

Figure 2: Integration limits – Wrobel method

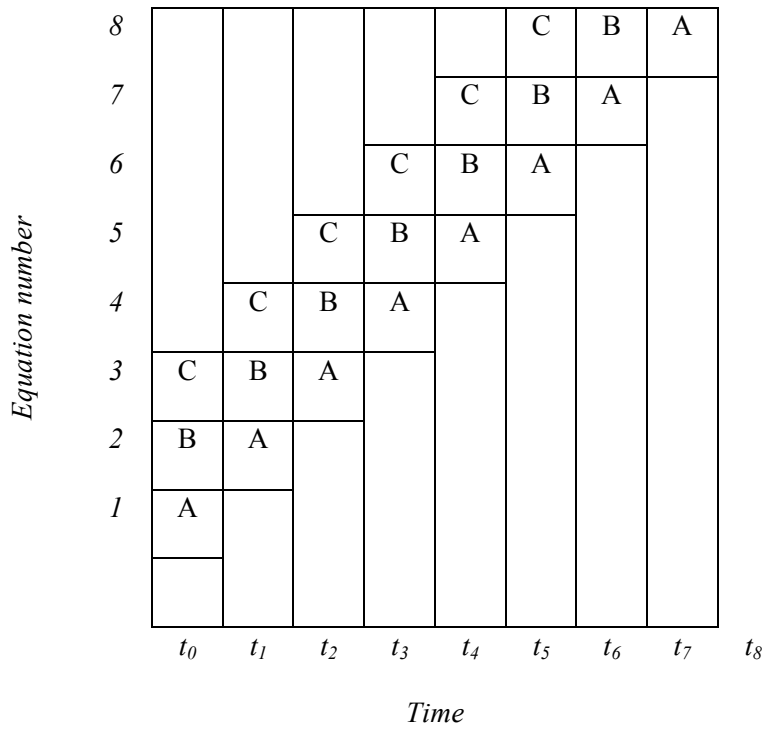

Figure 3: Integration limits – time truncation method with $m = 3$**.**

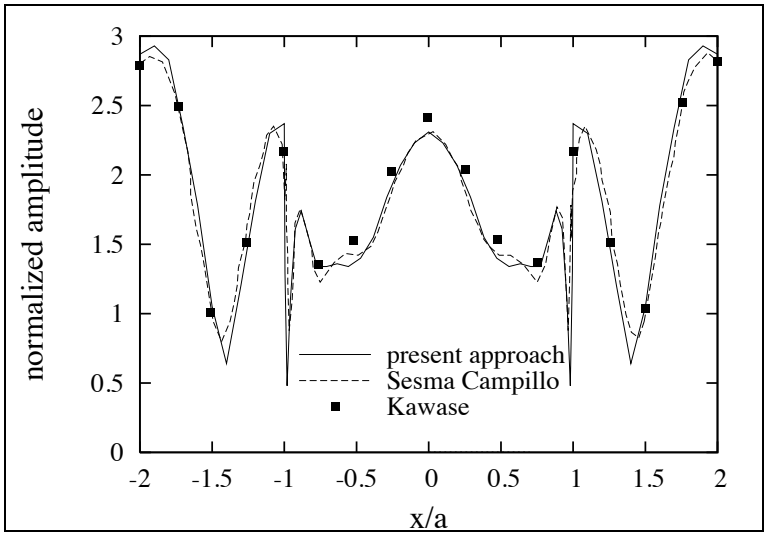

a. Horizontal displacements

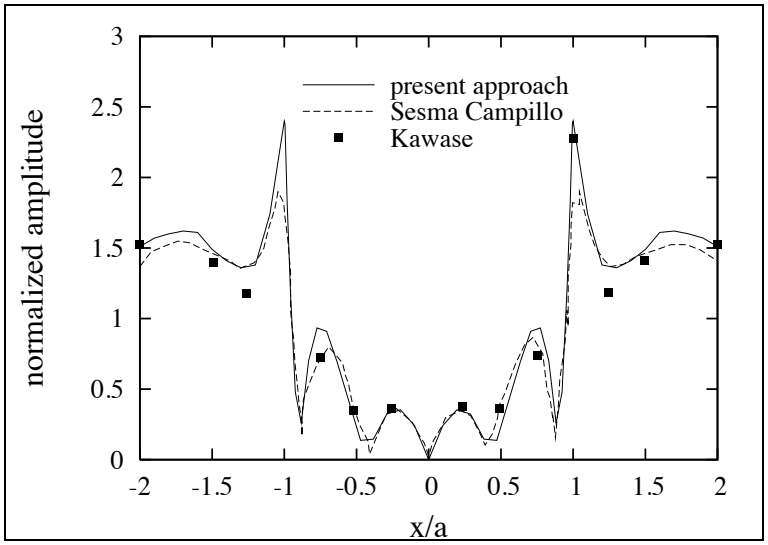

b. Vertical displacements

Figure 4: Normalized displacement amplitudes for vertical incidence of a harmonic plane SV wave upon a semi-circular canyon.

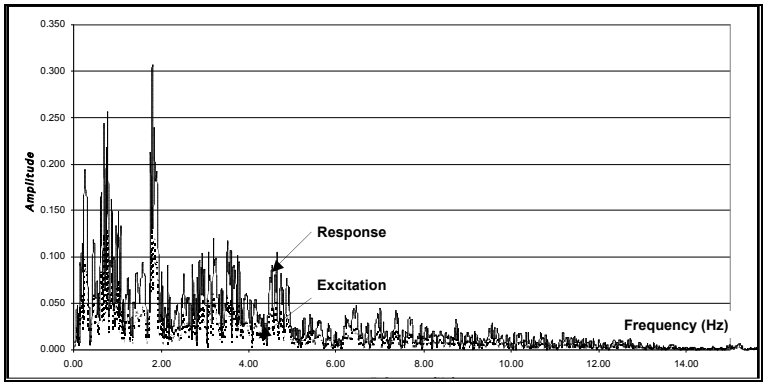

Figure 5: Test of the response of a free surface submitted to a real seismic excitation – Amplitudes of Fourier transforms of horizontal superficial displacements

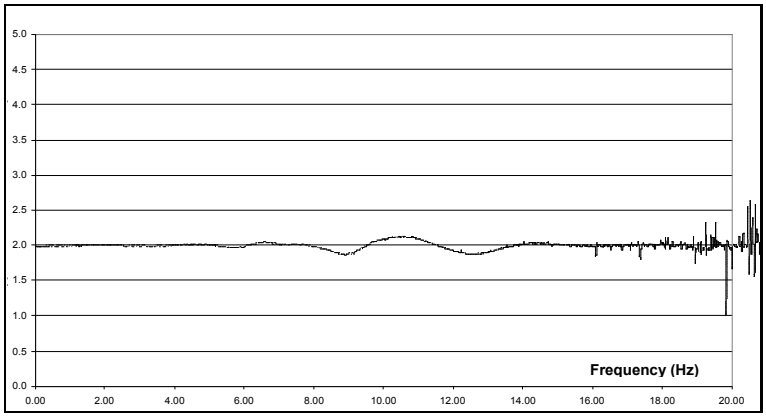

Figure 6: Ratio of the Fourier transform of the response of a free surface to the Fourier transform of the incident seismic excitation

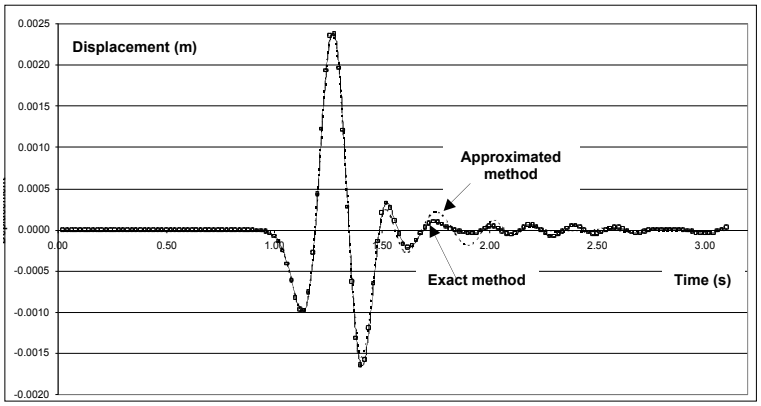

Figure 7: Comparison of approximated and exact methods on the axis of the trapezium

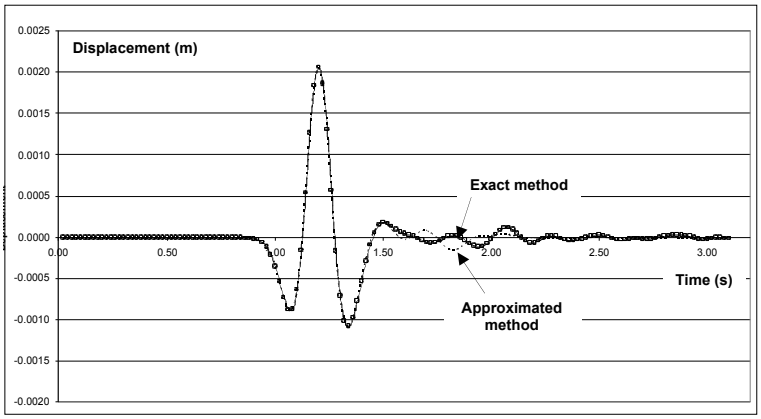

Figure 8: Comparison of approximated and exact methods at an edge of the ridge

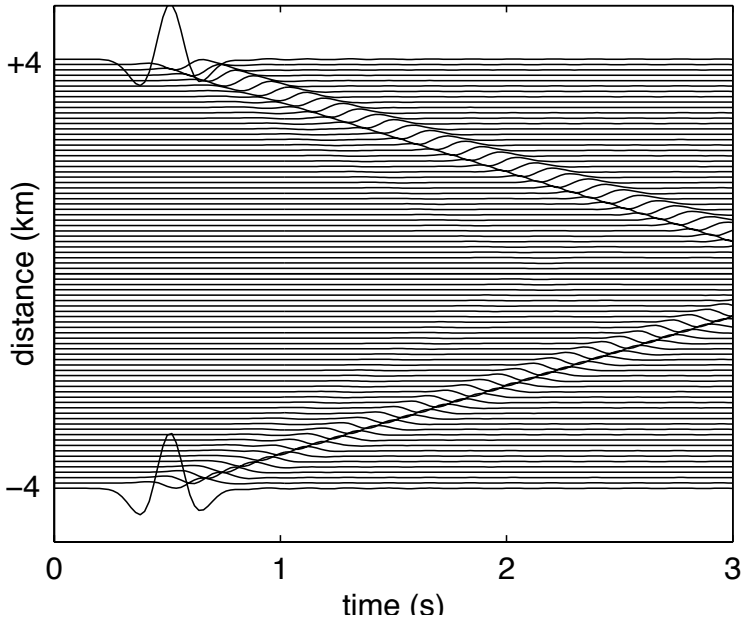

a. Traditional method

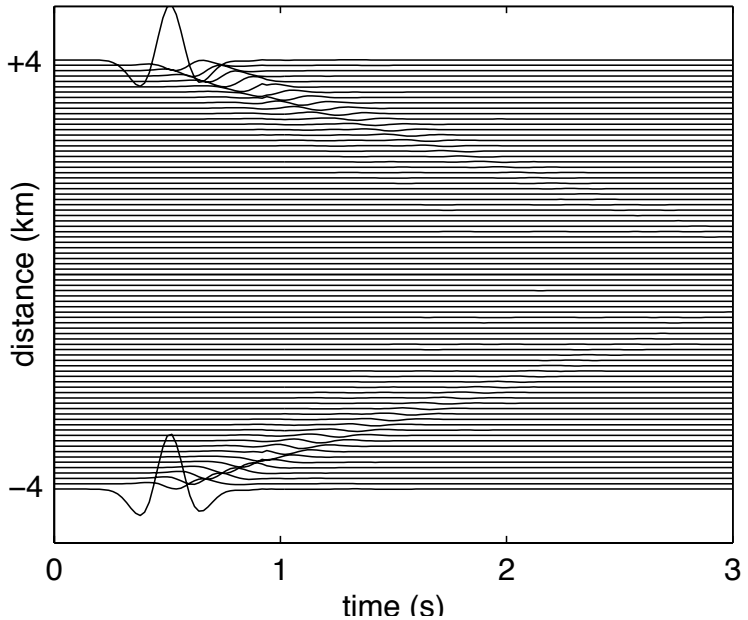

b. Time truncation technique

Figure 9: Propagation of artificial waves in half-plane problems in a traditional modelling (a) and with the time truncation technique (b)

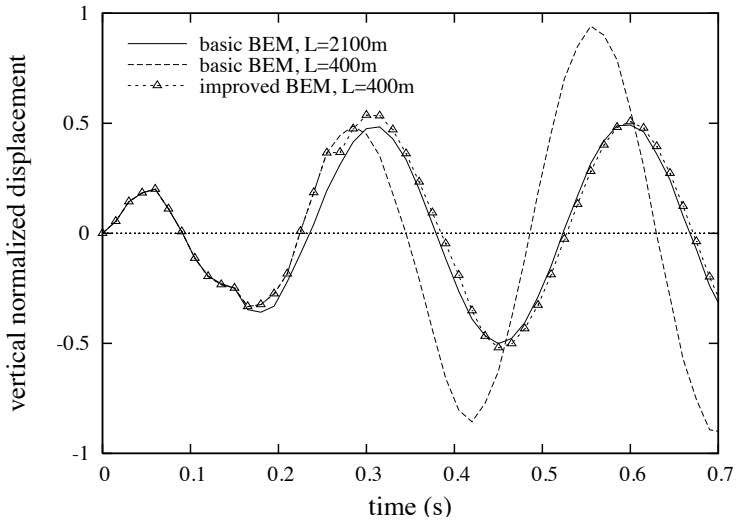

Figure 10: Effect of spatial truncation of the BE mesh for a half-plane problem

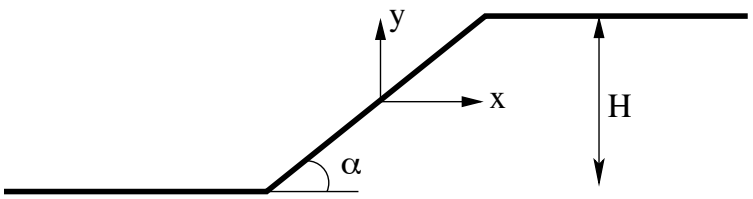

a.

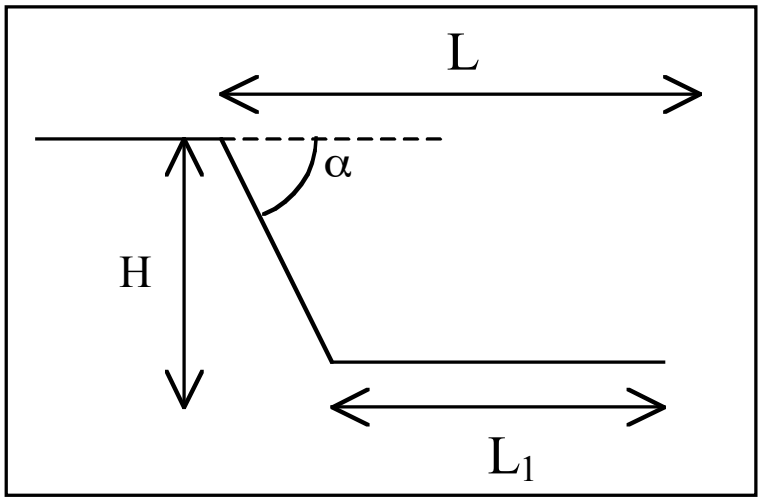

b.

Figure 11: Main geometrical parameters characterizing site irregularities: a. Slopes; b. Valleys. Due to symmetries, only the half of the valley is represented.

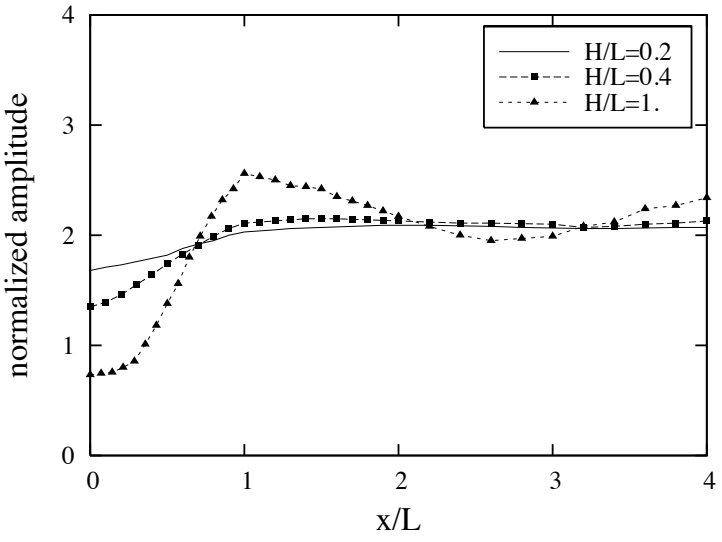

a. Triangular canyons

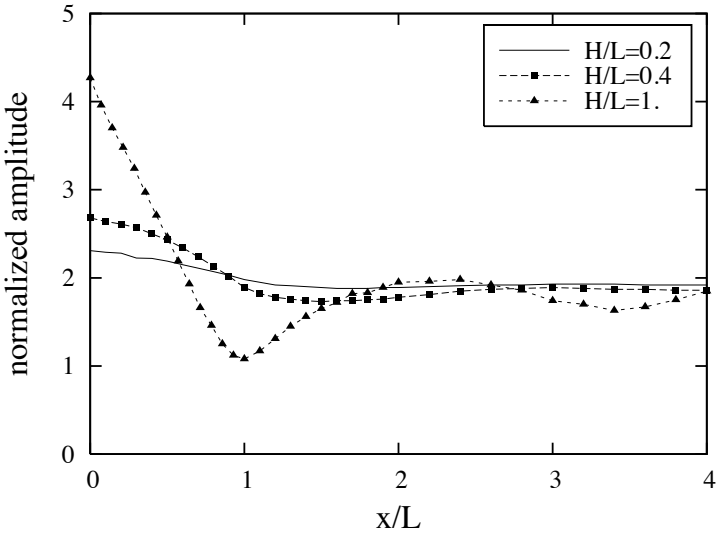

b. Triangular ridges

Figure 12: Comparison of the amplification spectra of horizontal displacements for canyons and ridges ($\eta = 0{,}5$)

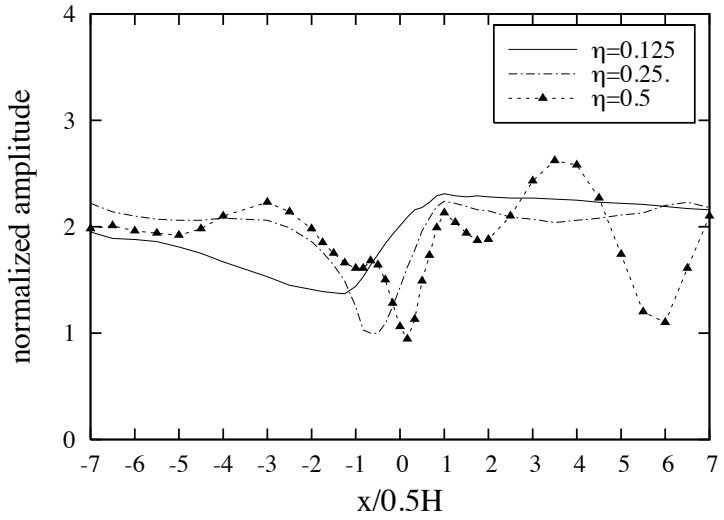

a. *ux*, slope

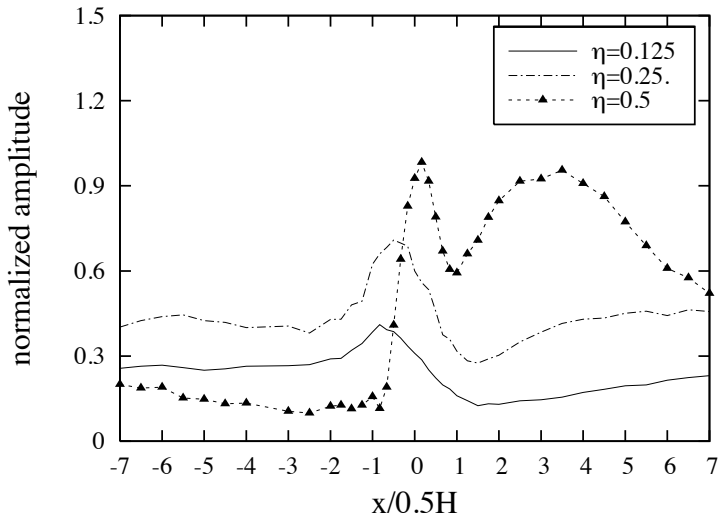

b. *uy*, slope

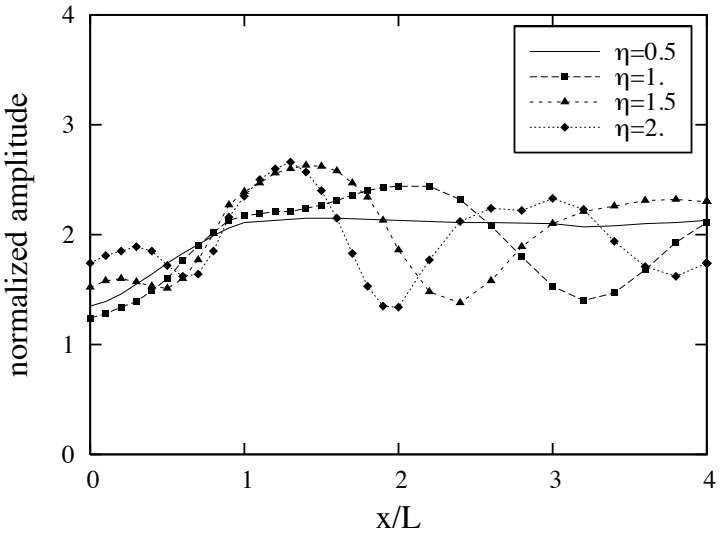

c. *ux*, triangular canyon

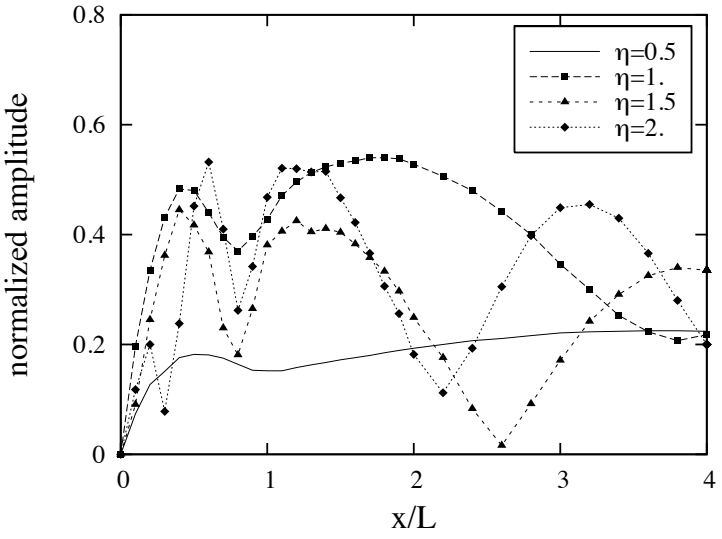

d. *uy*, triangular canyon

Figure 13: Normalized horizontal displacements (a; c) and vertical components (b; d) for a 45° slope (a; b) and a triangular canyon (c; d) for diverse dimensionless frequencies

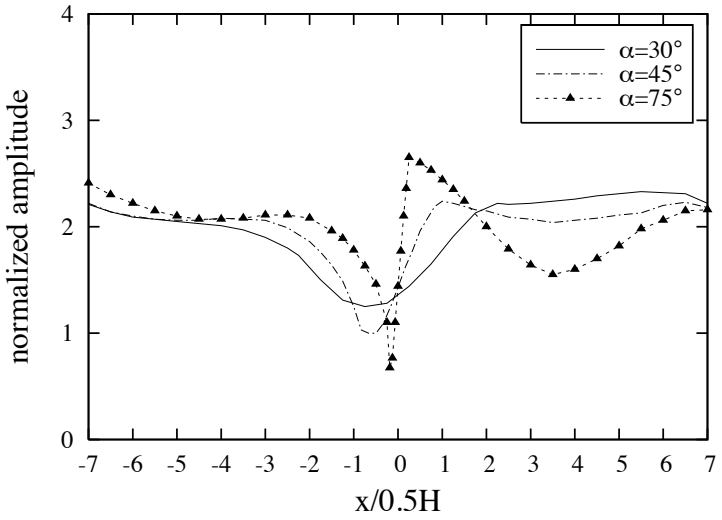

a. Horizontal component

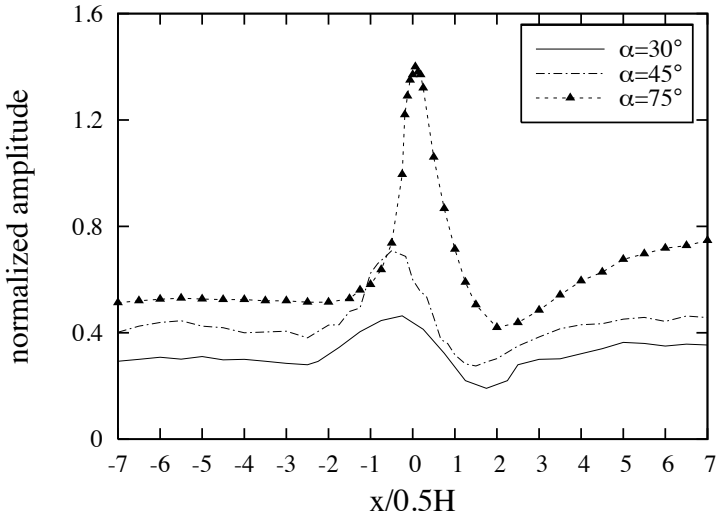

b. Vertical component

Figure 14: Influence of the slope inclination angle α on the seismic response of slopes ($\eta = 0{,}25$)

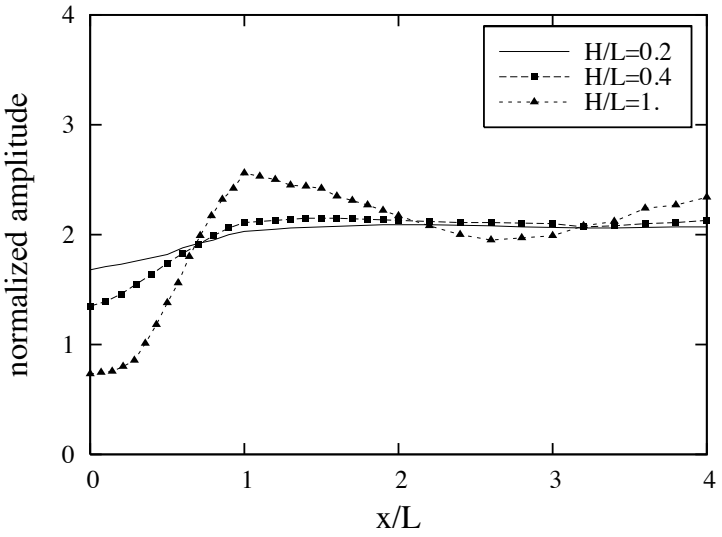

a. Horizontal component

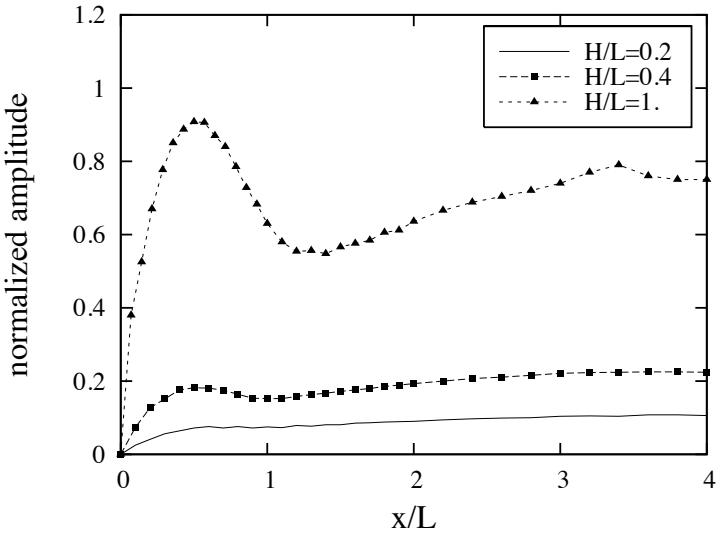

b. Vertical component

Figure 15: Influence of depth on the seismic response of triangular canyons ($\eta = 0{,}5$)

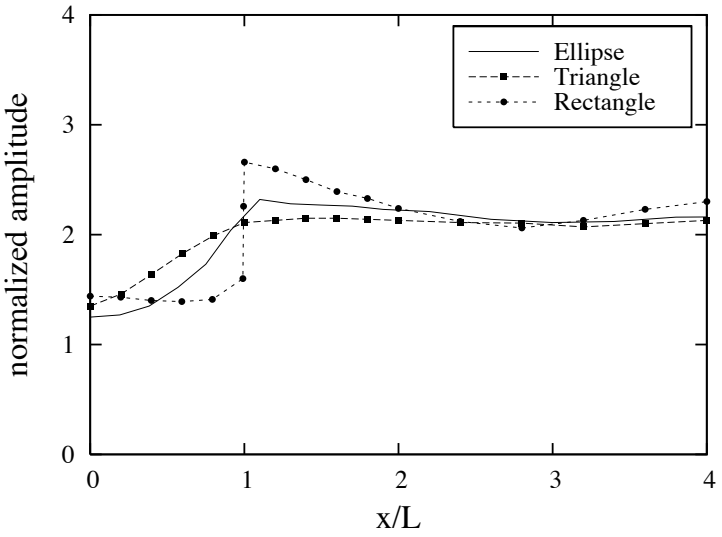

a. Horizontal component

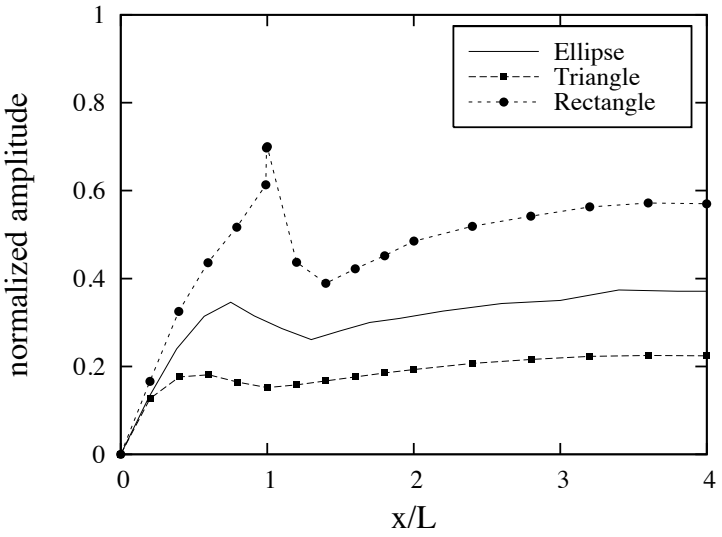

b. Vertical component

Figure 16: Influence of shape on the seismic response of shallow canyons (*H/L* = 0,4) at a low frequency ($\eta = 0{,}5$)